Robust Tightly Coupled UWB-ODO-Inertial Navigation in Complex Indoor Environments

Shuangyan Liu, Mingyang Liu, Hailiang Tang, Tisheng Zhang, *Member, IEEE*, Man Yuan, Xin Ding, and Xiaoji Niu, *Member, IEEE*

***Abstract*—In complex indoor environments, ultrawideband (UWB) technology can be used to achieve continuous absolute positioning. However, its accuracy is often degraded by non-line-of-sight (NLOS) signal interference. In this article, we propose a robust UWB-odometer (ODO)-inertial navigation system, named MODR-UOINS, to meet the high-accuracy positioning requirements for wheeled robots. Multisensor observations are tightly fused using the multistate constraint Kalman filter (MSCKF) framework, enabling efficient management of historical states. The proposed method can also mitigate accuracy degradation by fully using the short-term accuracy of ODO/inertial navigation system (INS) odometry, especially when the base stations are sparsely deployed. Meanwhile, a robust multiepoch outlier detection and rejection (MODR) algorithm based on random sample consensus (RANSAC) is introduced to detect and reject NLOS outliers effectively. Specifically, the high-accuracy short-term relative poses derived from ODO/INS odometry are utilized to evaluate the consistency of multiepoch UWB ranges. Experiment results demonstrate that the proposed MODR-UOINS achieves a positioning accuracy of 0.1 m in the open LOS environment and 0.15 m in the complex indoor NLOS environment. In addition, MODR-UOINS achieves an accuracy of about 0.17 m even when only two UWB base stations are available, exhibiting superior robustness.**

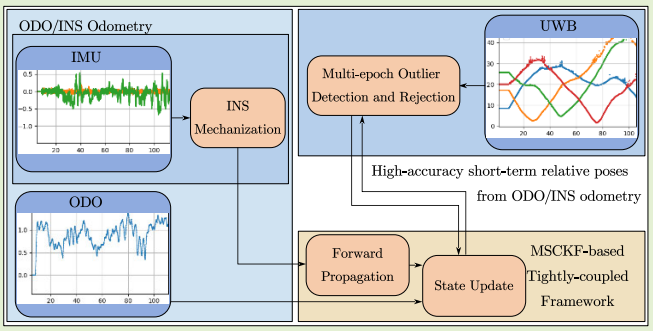

***Index Terms*—Multiepoch outlier detection and rejection (MODR), multisensor fusion navigation, non-line-of-sight (NLOS) mitigation, tightly coupled positioning, ultrawideband (UWB).**

I. Introduction

GLOBAL navigation satellite system (GNSS) is widely utilized in outdoor positioning scenarios [1]. However, satellite signals are often blocked in indoor environments, making GNSS unavailable. Ultrawideband (UWB) technology enables accurate indoor positioning by calculating distances based on signal propagation time [2]. Nevertheless, UWB signals are susceptible to obstruction and interference in complex indoor environments. Therefore, a dense deployment of UWB base stations is required in large indoor areas, such as underground parking garages and airports, so as to ensure continuous and reliable positioning. The microelectromechanical system (MEMS) inertial measurement unit (IMU) can provide motion data independently [3] and is widely used in practical scenarios such as pedestrian navigation [4], medical diagnosis [5], and sports training [6]. Thus, the inertial navigation system (INS) constructed based on the IMU can provide short-term position estimates during UWB signal outages, enhancing positioning continuity and robustness. Hence, the integration of UWB and MEMS IMU is widely used for indoor positioning, particularly for wheeled robots, which are commonly used in indoor positioning due to their simple structure and high control precision. Despite these advantages, a low-cost MEMS IMU is prone to accumulated errors, leading to degraded positioning accuracy [7]. Therefore, relying solely on UWB

Received 19 November 2025; accepted 22 December 2025. Date of publication 1 January 2026; date of current version 2 February 2026. This work was supported in part by the National Natural Science Foundation of China under Grant 42374034 and Grant 42504027, in part by the Key Research and Development Program of Hubei Province under Grant 2024BAB024, in part by the Major Program (JD) of Hubei Province under Grant 2023BAA02602, and in part by the High Quality Development Project of the Ministry of Industry and Information Technology (MIIT) under Grant 2024-182. The associate editor coordinating the review of this article and approving it for publication was Dr. Zengke Li. *(Corresponding authors: Hailiang Tang; Xiaoji Niu.)*

Shuangyan Liu and Hailiang Tang are with the GNSS Research Center and the Electronic Information School, Wuhan University, Wuhan 430079, China (e-mail: liushuangyan@whu.edu.cn; thl@whu.edu.cn).

Mingyang Liu is with the College of Geodesy and Geomatics, Shandong University of Science and Technology, Jinan 266590, China (e-mail: 202383020137@sdust.edu.cn).

Tisheng Zhang and Xiaoji Niu are with the GNSS Research Center, Wuhan University, Wuhan 430079, China, and also with Hubei Luojia Laboratory, Wuhan 430079, China (e-mail: zts@whu.edu.cn; xjniu@whu.edu.cn).

Man Yuan and Xin Ding are with the GNSS Research Center, Wuhan University, Wuhan 430079, China (e-mail: yuanman@whu.edu.cn; dingxin@whu.edu.cn).

Digital Object Identifier 10.1109/JSEN.2025.3648139

and MEMS IMU for positioning is not enough in complex indoor environments.

To solve the above problem, we equip wheeled robots with wheel odometer (ODO) as auxiliary sensors, which offers advantages such as autonomy and low cost compared to other onboard sensors, and can effectively mitigate IMU drift [8], [9], [10]. On this basis, this article proposes a robust tightly coupled UWB-ODO-INS, named MODR-UOINS. By tightly integrating UWB, ODO, and IMU, reliable positioning can be maintained even when UWB base stations are sparsely deployed. Meanwhile, the short-term high-accuracy relative poses from ODO/INS odometry provide robust geometric constraints to verify the consistency of multiepoch UWB ranges. Hence, a multiepoch outlier detection and rejection (MODR) strategy for UWB ranges based on random sample consensus (RANSAC) [11] is proposed, which does not require absolute poses. It uses recursive relative poses from ODO/INS odometry to estimate the base station positions following the model in Section V-A. Residuals of the UWB ranges at each epoch are then calculated based on the estimated positions. The consistency of the current UWB range is evaluated by checking whether its residual is below a preset threshold, thereby enabling outlier detection. Meanwhile, the multistate constraint Kalman filter (MSCKF) can maintain constraints among historical states, thereby enabling the implementation of the proposed MODR method. Thus, MODR-UOINS is formulated based on the MSCKF. The main contributions of this article are given as follows.

1) We propose a tightly coupled UWB-ODO-inertial navigation method based on the MSCKF framework. Furthermore, UWB scale factors and offsets are incorporated to estimate and calibrate hardware-induced ranging errors online, enhancing positioning accuracy.
2) To mitigate UWB non-line-of-sight (NLOS) effects, an MODR method is proposed, which does not rely on absolute pose accuracy. Specifically, a RANSAC-based method is employed to verify the consistency of multiepoch UWB ranges by leveraging short-term relative poses from ODO/INS odometry.
3) Comprehensive experiments were conducted in LOS and NLOS environments. MODR-UOINS achieves about 0.15-m positioning accuracy in the complex indoor NLOS environment, which is comparable to that in the open LOS environment. Besides, MODR-UOINS still achieves an accuracy of about 0.17 m when using only two base stations, demonstrating superior robustness.

II. Related Work

Current UWB/IMU fusion systems are typically classified into loosely coupled and tightly coupled architectures. In loosely coupled systems, navigation outputs from UWB are integrated with IMU data through relatively simple methods. Sharifuzzaman Sagar et al. [12] proposed a loosely coupled UWB/IMU relative positioning system. In this system, moving average and min–max removing preprocessing filters were used to reduce noise effects on UWB ranges. Zhong et al. [13] proposed a loosely coupled method based on the extended Kalman filter (EKF), leveraging the complementary characteristics of UWB and IMU to enhance positioning accuracy. Naheem and Kim [14] removed partial UWB ranging outliers by analyzing the deviation between UWB-derived and IMU-predicted positions. In [15], a two-stage Kalman filter-based approach was proposed to estimate the attitude and position of the robot. However, loosely coupled systems require dense base station deployment to maintain positioning stability and are less effective in mitigating NLOS effects on UWB ranging.

In tightly coupled systems, raw UWB measurements are directly fused with IMU data, enabling the use of available measurements even under partial signal loss and, thereby, improving the robustness of the positioning system. Various methods have been explored, including those based on the EKF [16], the unscented Kalman filter [17], the backpropagation neural network [18], and machine learning models [19]. However, the above methods do not explicitly address UWB NLOS conditions or rely solely on simple threshold-based detection [14]. This limits their effectiveness in complex environments. To address this, many studies have proposed outlier culling methods to mitigate UWB NLOS. Chen and Li [20] used high-accuracy short-term IMU data to compensate for UWB NLOS errors, while UWB measurements corrected IMU drift. In [21], fuzzy comprehensive evaluation and semidefinite programming were used to detect and reject NLOS outliers. Furthermore, deep learning-based methods have been explored. Zheng et al. [22] used convolutional neural networks to analyze UWB data to identify NLOS signals. Fontaine et al. [23] used autoencoders to detect NLOS conditions. However, these methods rely only on single-epoch UWB ranges for outlier detection, limiting robustness in complex indoor NLOS environments.

Therefore, multiepoch outlier culling strategies have been introduced into UWB-based fusion positioning schemes to better suppress NLOS effects. Zhu et al. [24] identified and suppressed NLOS by analyzing changes in UWB ranging measurements at adjacent time steps, combined with short-term pose constraints provided by IMU. In [25], a differential distance sliding window scheme was designed to detect NLOS in multiepoch UWB ranging measurements and reject the resulting ranging outliers. However, these methods exclusively fuse MEMS IMU and UWB data, and MEMS IMU has significant errors, with its accuracy degrading during long-term navigation [7].

To further enhance the robustness and accuracy of UWB/IMU fusion systems in NLOS environments, multisensor fusion navigation approaches have been explored. Additional sensors, such as light detection and ranging (LiDAR), have been integrated. Zhang et al. [26] proposed a tightly coupled UWB/LiDAR/IMU framework, where a multiepoch outlier rejection method was used to enhance positioning accuracy. However, LiDAR is expensive, computationally demanding, and sensitive to dynamic occlusions. Chen et al. [27] identified NLOS signals using laser point cloud maps and applied a gray forecast model to correct them based on multiepoch UWB ranges. The cor-

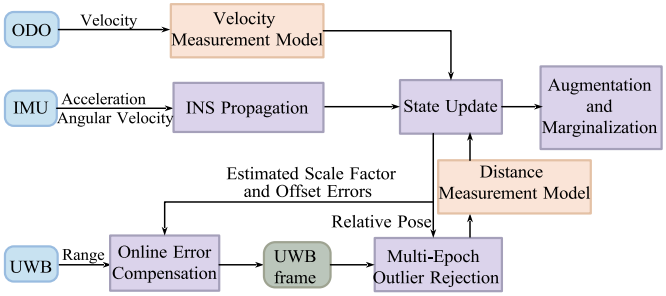

Fig. 1. System overview of the proposed MODR-UOINS.

rected data were then fused via factor graph optimization. However, factor graph optimization is computationally expensive. In addition, the gray forecast model requires high-quality historical data, which is often unavailable in real-world environments.

III. System Overview

The proposed system tightly integrates UWB, ODO, and IMU measurements within an IMU-centric state estimation framework, as shown in Fig. 1. First, the INS propagation step is executed: the prior pose information is obtained through IMU mechanization, and the state vector and covariance matrix are propagated, respectively. Once ODO measurements are received, they are used to construct a velocity measurement model and update the current state. This mitigates IMU drift and improves the short-term relative pose accuracy of the ODO/INS odometry. When UWB ranges from one measurement period are received, they are compensated using the online estimated systematic ranging bias, and the corrected ranges are treated as a new UWB frame. Then, the proposed RANSAC-based MODR method is applied to process UWB ranges within the window if the number of UWB frames in the sliding window reaches the predefined threshold. The good-quality UWB measurements are then used to update the MSCKF state, enabling pose correction, as well as compensation for both IMU and UWB system errors. After the state update, the corrected current IMU pose is augmented into the MSCKF state vector for the next state update. Finally, the earliest UWB frame is marginalized once the number of UWB frames exceeds the window length to bound the computational complexity.

IV. Tightly Coupled UWB-ODO-Inertial Fusion Based on MSCKF

By tightly coupling UWB, ODO, and IMU measurements, reliable positioning can be achieved even under sparse UWB base station deployment. Here, we employ the famous MSCKF for multisensor fusion, as its sliding-window structure enables efficient management of multiepoch measurements. In this section, the MSCKF state vector is first introduced, followed by the procedures of state augmentation and marginalization. Finally, the measurement models for UWB and ODO are presented, respectively.

A. State Vector

The MSCKF state vector is composed of three parts: the IMU error states, the systematic UWB ranging error states, and the UWB frame states, which are denoted as $\boldsymbol{X}_{\mathrm{IMU}}$, $\boldsymbol{X}_{\mathrm{UWB}}$, and $\boldsymbol{X}_{\mathrm{KFUWB}}$, respectively. The complete state vector is defined as

$$\boldsymbol{X} = \begin{bmatrix} \boldsymbol{X}_{\mathrm{IMU}}^T & \boldsymbol{X}_{\mathrm{UWB}}^T & \boldsymbol{X}_{\mathrm{KFUWB}}^T \end{bmatrix}^{\mathrm{T}} \tag{1}$$

where each subvector is specifically defined as follows:

$$\begin{aligned} \boldsymbol{X}_{\mathrm{IMU}} &= \begin{bmatrix} \delta\boldsymbol{\phi}_b^w & \delta\boldsymbol{p}_b^w & \delta\boldsymbol{v}_b^w & \delta\boldsymbol{b}_a & \delta\boldsymbol{b}_g \end{bmatrix}^{\mathrm{T}} \\ \boldsymbol{X}_{\mathrm{UWB}} &= [\delta\boldsymbol{s}_u, \delta\boldsymbol{b}_u]^{\mathrm{T}} \\ &= \left[\delta s_{u_1}\delta s_{u_2}, \ldots, \delta s_{u_r}, \delta b_{u_1}\delta b_{u_2}, \ldots, \delta b_{u_r}\right]^{\mathrm{T}} \\ \boldsymbol{X}_{\mathrm{KFUWB}} &= \begin{bmatrix} \boldsymbol{X}_{\mathrm{KFUWB},1} & \boldsymbol{X}_{\mathrm{KFUWB},2}, \ldots, \boldsymbol{X}_{\mathrm{KFUWB},N} \end{bmatrix}^{\mathrm{T}} \\ &= \Big[\left[\delta\boldsymbol{\phi}_{b_1}^w, \delta\boldsymbol{p}_{b_1}^w\right]^{\mathrm{T}}, \left[\delta\boldsymbol{\phi}_{b_2}^w, \delta\boldsymbol{p}_{b_2}^w\right]^{\mathrm{T}}, \ldots, \\ &\qquad \left[\delta\boldsymbol{\phi}_{b_N}^w, \delta\boldsymbol{p}_{b_N}^w\right]^{\mathrm{T}} \Big] \end{aligned} \tag{2}$$

where b and w represent the IMU frame and the world frame, respectively. $\delta\boldsymbol{\phi}_b^w$, $\delta\boldsymbol{p}_b^w$, and $\delta\boldsymbol{v}_b^w$ are the attitude, position, and velocity errors of the IMU, respectively. $\delta\boldsymbol{b}_a$ and $\delta\boldsymbol{b}_g$ represent the accelerometer bias errors and gyroscope bias errors, respectively, which are modeled as first-order Gaussian Markov processes to capture their slow variations over time. δs_{u_i} and δb_{u_i} are the scale factor error and offset error of the ith UWB base station, respectively, which are mainly caused by hardware factors such as clock frequency drift and antenna delay. These errors are modeled as random constants and introduced into the state vector to compensate for systematic UWB ranging errors, and thus, the positioning accuracy can be improved. r indicates the number of UWB base stations in the system. $\delta\boldsymbol{\phi}_{b_k}^{\omega}$ and $\delta\boldsymbol{p}_{b_k}^{\omega}$ are the attitude error and position error of the IMU at time t_k, respectively, and N is the sliding window length of MSCKF. By augmenting $\boldsymbol{X}_{\mathrm{KFUWB}}$ into the state vector, these states are jointly estimated and updated using the refined UWB ranging values.

The attitude error is defined as

$$\mathbf{R} = \hat{\mathbf{R}}\,\mathrm{Exp}(\delta\boldsymbol{\phi}) \approx \hat{\mathbf{R}}\,(\mathbf{I} + [\delta\boldsymbol{\phi}]_{\times}) \tag{3}$$

where $\mathbf{R}$ and $\hat{\mathbf{R}}$ are the true attitude and the estimated attitude, respectively. $\mathrm{Exp}(\cdot)$ represents the exponential map operation, $\mathbf{I}$ is the identity matrix, and $[\cdot]_{\times}$ is the skew-symmetric matrix operator [28]. The definition of position error, velocity error, UWB scale factor error, and UWB offset error is given as follows:

$$\delta\boldsymbol{x} = \boldsymbol{x} - \hat{\boldsymbol{x}} \tag{4}$$

where $\delta\boldsymbol{x}$, $\boldsymbol{x}$ and $\hat{\boldsymbol{x}}$ represent the error, true, and estimated state, respectively.

When IMU measurements are available, high-frequency poses are produced through INS mechanization. INS mechanization refers to the equations for updating the attitude, velocity, and position of the robot. The corresponding equations are given as follows:

$$\begin{aligned} \mathbf{R}_{b_{k+1}}^w &= \mathbf{R}_{b_k}^w \mathrm{Exp}\left(\boldsymbol{\omega}_k^b \Delta t\right) \\ \boldsymbol{v}_{b_{k+1}}^w &= \boldsymbol{v}_{b_k}^w + \mathbf{R}_{b_k}^w \boldsymbol{f}_k^b \Delta t + \boldsymbol{g}_k^w \Delta t \\ \boldsymbol{p}_{b_{k+1}}^w &= \boldsymbol{p}b_k{}^w + \boldsymbol{v}_{b_k}^w \Delta t \end{aligned} \tag{5}$$

where $\mathbf{R}_{b_k}^w$, $\boldsymbol{v}_{b_k}^w$ and $\boldsymbol{p}_{b_k}^w$ are the attitude, velocity, and position of the IMU at time, respectively. $\boldsymbol{f}_k^b$ and $\boldsymbol{\omega}_k^b$ represent the acceleration and angular velocity of the IMU at time t_k. Δt is the time interval. $\boldsymbol{g}_k^w$ is the gravitational acceleration in the w frame.

B. State Augmentation and Marginalization

When the high-frequency pose information from IMU mechanization is obtained, the state vector and the covariance matrix are propagated forward using the standard error-state Kalman filter (ESKF) prediction equations [29]. Unlike the standard ESKF with a fixed state dimension, the adopted MSCKF maintains a dynamically changing state vector through augmentation and marginalization. This sliding-window strategy helps achieve the proposed MODR method, thereby enhancing the overall robustness.

Specifically, when a new UWB frame is received, the IMU states are corrected. The corresponding IMU pose is then augmented into the state vector, while the covariance matrix is augmented. Assuming that the current state dimension is n, the augmented state dimension is m, and the Jacobian matrix of the augmented state with respect to the current state is $\mathbf{J}_{m\times n}$. The augmented state covariance matrix can be written as

$$\mathbf{P}_{(n+m)\times(n+m)} = \begin{bmatrix} \mathbf{P}_{n\times n} & \mathbf{P}_{n\times n}\left(\mathbf{J}^T\right)_{n\times m} \\ \mathbf{J}_{m\times n}\mathbf{P}_{n\times n} & \mathbf{J}_{m\times n}\mathbf{P}_{n\times n}\left(\mathbf{J}^T\right)_{n\times m} \end{bmatrix}. \quad (6)$$

When the number of UWB frames exceeds the allowed maximum, the marginalization is performed. The states associated with the earliest frame and the corresponding rows and columns of the covariance matrix are deleted.

C. UWB Range Measurement Model

The UWB module, based on the DW1000 chip, employs the double-sided two-way ranging (DS-TWR) method [30] to estimate distance from time-of-arrival (TOA) measurements [31]. The residual is obtained by calculating the measured distance from the UWB base station with the predicted range. For instance, the residual of the range measurement $d_{i,k}$ from the ith UWB base station at time t_k is defined as

$$\begin{aligned} \boldsymbol{r}_{i,k} &= s_{u_i} \cdot \left\| \boldsymbol{p}_{\text{ant}}^w - \boldsymbol{p}_{u_i}^w \right\| + b_{u_i} - d_{i,k} \\ &= s_{u_i} \cdot \left\| \boldsymbol{p}_{b_k}^w + \mathbf{R}_{b_k}^w \boldsymbol{p}_{\text{ant}}^b - \boldsymbol{p}_{u_i}^w \right\| + b_{u_i} - d_{i,k} \end{aligned} \quad (7)$$

where s_{u_i} and b_{u_i} are the scale factor and offset of the ith UWB base station, respectively. $\boldsymbol{p}_{\text{ant}}^w$ is the position of the UWB antenna in the w frame. $\boldsymbol{p}_{b_k}^w$ and $\mathbf{R}_{b_k}^w$ are the position and attitude of the IMU in the w frame at time t_k, respectively. $\boldsymbol{p}_{\text{ant}}^b$ is the position of the UWB antenna in the b frame (i.e., the UWB lever arm). $\boldsymbol{p}_{u_i}^w$ is the position of the ith UWB base station in the w frame. The Jacobian matrix of the residual can be written as

$$\boldsymbol{H} = \begin{bmatrix} \dfrac{\partial \boldsymbol{r}_{i,k}}{\partial \boldsymbol{X}_{\text{IMU}}} & \dfrac{\partial \boldsymbol{r}_{i,k}}{\partial \boldsymbol{X}_{\text{UWB}}} & \dfrac{\partial \boldsymbol{r}_{i,k}}{\partial \boldsymbol{X}_{\text{KFUWB}}} \end{bmatrix} \quad (8)$$

and the specific form of each term is given as follows:

$$\begin{aligned} \frac{\partial \boldsymbol{r}_{i,k}}{\partial \boldsymbol{X}_{\text{IMU}}} &= 0_{1\times 15} \\ \frac{\partial \boldsymbol{r}_{i,k}}{\partial \boldsymbol{X}_{\text{UWB}}} &= \begin{bmatrix} \dfrac{\partial \boldsymbol{r}_{i,k}}{\partial \boldsymbol{s}_u}, \dfrac{\partial \boldsymbol{r}_{i,k}}{\partial \boldsymbol{b}_u} \end{bmatrix} \\ \frac{\partial \boldsymbol{r}_{i,k}}{\partial \boldsymbol{s}_{u_j}} &= \begin{cases} \left\| \boldsymbol{p}_{\text{ant}}^w - \boldsymbol{p}_{u_i}^w \right\|, & j = i \\ 0, & j \neq i \end{cases} \\ \frac{\partial \boldsymbol{r}_{i,k}}{\partial \boldsymbol{b}_{u_j}} &= \begin{cases} 1, & j = i \\ 0, & j \neq i \end{cases} \\ \frac{\partial \boldsymbol{r}_{i,k}}{\partial \boldsymbol{X}_{\text{KFUWB},j}} &= \begin{cases} -\begin{bmatrix} \boldsymbol{s}_{u_i} \dfrac{\left(\boldsymbol{p}_{\text{ant}}^w - \boldsymbol{p}_{u_i}^w\right)^{\mathrm{T}}}{\left\| \boldsymbol{p}_{\text{ant}}^w - \boldsymbol{p}_{u_i}^w \right\|^{\mathrm{T}}} \mathbf{R}_{b_k}^{\omega} \left(\boldsymbol{p}_{\text{ant}}^b\right) \\ \boldsymbol{s}_{u_i} \dfrac{\left(\boldsymbol{p}_{\text{ant}}^w - \boldsymbol{p}_{u_i}^w\right)^{\mathrm{T}}}{\left\| \boldsymbol{p}_{\text{ant}}^w - \boldsymbol{p}_{u_i}^w \right\|^{\mathrm{T}}} \end{bmatrix}^{\mathrm{T}}, & j = k \\ 0_{6\times 1}, & j \neq k. \end{cases} \end{aligned} \quad (9)$$

The residual vector $\boldsymbol{r}^{\text{UWB}}$ and the Jacobian matrix $\mathbf{H}^{\text{UWB}}$ are obtained by rowwise stacking of the residuals and Jacobians from multiple epochs and are then used for the state update.

D. ODO Velocity Measurement Model

In the ODO measurement model, the velocity residual is defined as the difference between the ODO-measured robot velocity and the estimated robot velocity

$$\boldsymbol{r}_{\text{odo}} = \mathbf{R}_b^s \mathbf{R}_v^b \boldsymbol{v}_{\text{odo}} - \left(\boldsymbol{v}_b^w - \mathbf{R}_b^w \left[\boldsymbol{l}_{\text{odo}} \times \boldsymbol{\omega}^b \right] \right) \quad (10)$$

where $\mathbf{R}_v^b$ is the direction cosine matrix (DCM) between the b frame and the vehicle frame, $\boldsymbol{v}_{\text{odo}}$ is the velocity measured by the ODO, and $\boldsymbol{v}_b^w$ is the velocity estimated by the IMU. $\boldsymbol{l}_{\text{odo}}$ is the lever arm vector from the IMU to the ODO, $\boldsymbol{\omega}^b$ is the current angular velocity of the IMU, and $\times$ represents the cross-product operator. The specific form of $\boldsymbol{v}_{\text{odo}}$ is given as follows:

$$\boldsymbol{v}_{\text{odo}} = \begin{bmatrix} v_x & 0 & 0 \end{bmatrix} \quad (11)$$

where v_x is the forward velocity measurement of the ODO, with backward and lateral velocities modeled as zero, reflecting the nonholonomic constraint (NHC) [9]. Based on this ODO velocity measurement model, the robot motion is continuously constrained by forward velocity measurements and NHCs. As a result, the velocity and attitude errors of the IMU are corrected, thereby effectively limiting MEMS IMU drift.

The Jacobian matrix of the ODO velocity residual with respect to $\boldsymbol{X}_{\text{IMU}}$ is given as follows:

$$H = \begin{bmatrix} 0_{3\times 3}, \mathbf{I}_{3\times 3}, \mathbf{R}_b^w \left(\boldsymbol{l}_{\text{odo}} \times \boldsymbol{\omega}^b \right)_{\times}, 0_{3\times 3}, \mathbf{R}_b^w \left(\boldsymbol{l}_{\text{odo}} \right)_{\times} \end{bmatrix}. \quad (12)$$

V. RANSAC-Based MODR for UWB Ranges

The ODO/INS odometry can achieve high-accuracy short-term relative poses, which can be used to estimate the

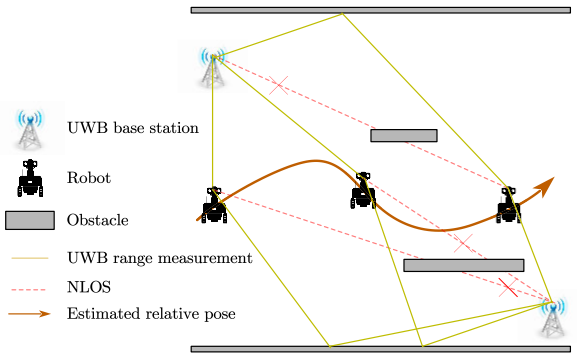

Fig. 2. Schematic of multiepoch UWB measurements.

positions of base stations. Based on the estimated positions, the theoretical ranges for each UWB measurement can be calculated, and the corresponding residuals can be obtained. By examining whether these residuals are below a preset threshold, the consistency of multiepoch UWB ranges can be verified, thereby enabling RANSAC-based outlier rejection. In this section, the estimation model of the UWB base station is introduced first, and then, the MODR method based on RANSAC is presented.

A. Estimation Model of UWB Base Station

The schematic of multiepoch UWB measurements is shown in Fig. 2. The relative position of the base station can be estimated by constructing a nonlinear objective function, expressed as

$$F\left(\boldsymbol{p}_{u_i}^{w}\right)=\min_{\boldsymbol{p}_{u_i}^{w}}\sum_{j=1}^{N}\left(\left\|\boldsymbol{p}_{b_j}^{w}+\mathbf{R}_{b_j}^{w}\boldsymbol{p}_{\text{ant}}^{b}-\boldsymbol{p}_{u_i}^{w}\right\|-d_{i,j}\right)^2. \quad (13)$$

The Levenberg–Marquardt (LM) algorithm [32] is employed to solve the equation. The detailed solution steps are given as follows.

Step 1: Select an initial point $\boldsymbol{p}_{u_i}^{w,(0)}$; initialize the maximum number of iterations K, the threshold ε, and the damping factor $\lambda^{(0)}$; and set the current iteration count $k=0$.

Step 2: Calculate the residual of $d_{i,j}$, and denote it by $\boldsymbol{r}_j^{(k)}$:

$$\boldsymbol{r}_j^{(k)}=\left\|\boldsymbol{p}_{b_j}^{w}+\mathbf{R}_{b_j}^{w}\boldsymbol{p}_{\text{ant}}^{b}-\boldsymbol{p}_{u_i}^{w,(k)}\right\|-d_{i,j}.$$

Step 3: Calculate the Jacobian matrix of $d_{i,j}$, and denote it by:

$$\mathbf{J}_j^{(k)}:\mathbf{J}_j^{(k)}=\frac{\partial \boldsymbol{r}_j^{(k)}}{\partial \boldsymbol{p}_{u_i}}=-\frac{\left(\boldsymbol{p}_{b_j}^{w}+\mathbf{R}_{b_j}^{w}\boldsymbol{p}_{\text{ant}}^{b}-\boldsymbol{p}_{u_i}^{w,(k)}\right)^{\mathrm{T}}}{\left\|\boldsymbol{p}_{b_j}^{w}+\mathbf{R}_{b_j}^{w}\boldsymbol{p}_{\text{ant}}^{b}-\boldsymbol{p}_{u_i}^{w,(k)}\right\|}.$$

Step 4: The residual vector and the Jacobian matrix can be obtained by concatenating all residuals and Jacobian matrices rowwise: $\boldsymbol{r}^{(k)}=[\boldsymbol{r}_1^{(k)}\ \boldsymbol{r}_2^{(k)}\ \cdots\ \boldsymbol{r}_N^{(k)}]^{\mathrm{T}}$ and $\mathbf{J}^{(k)}=[\mathbf{J}_1^{(k)}\ \mathbf{J}_2^{(k)}\ \cdots\ \mathbf{J}_N^{(k)}]^{\mathrm{T}}$.

Step 5: Calculate the position increment, and the formula is

$$\Delta\boldsymbol{p}_{u_i}^{w,(k)}=-\left(\mathbf{J}^{(k)T}\mathbf{J}^{(k)}+\lambda^{(k)}\mathbf{I}\right)^{-1}\mathbf{J}^{(k)T}\boldsymbol{r}^{(k)}.$$

Step 6: Update position: $\boldsymbol{p}_{u_i}^{w,(k+1)}=\boldsymbol{p}_{u_i}^{w,(k)}+\Delta\boldsymbol{p}_{u_i}^{w,(k)}$.

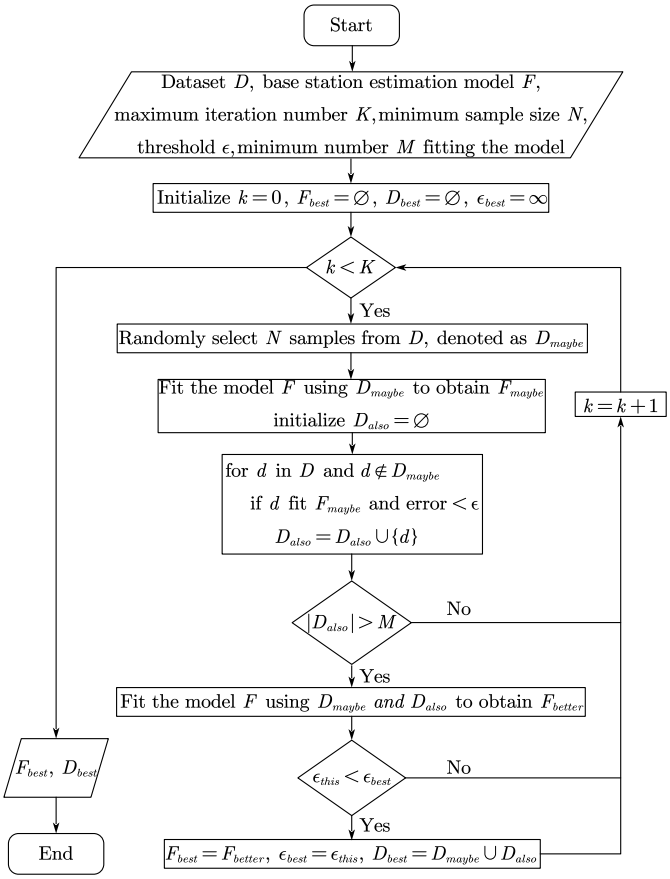

Fig. 3. Flowchart of the proposed RANSAC-based multiepoch outlier culling algorithm. N and M are set to 70% and 85% of the total number of ranges in D, respectively, and the threshold ϵ is set to 0.05 m.

Step 7: If $k>K$ or $\|\Delta\boldsymbol{p}_{u_i}^{w,(k)}\|<\varepsilon$, terminate the iteration; otherwise, update $k=k+1$, and return to Step 2.

Following these steps, the relative position of the base station $\boldsymbol{p}_{u_i}^{w}$ can be estimated.

B. MODR Based on RANSAC

In complex environments, UWB ranging measurements may be affected by NLOS, resulting in degraded positioning accuracy. Hence, based on the MSCKF sliding window strategy, a RANSAC-based MODR method is adopted to detect and reject outliers, which does not require absolute poses. This method utilizes the UWB ranges, and the recursive relative poses from ODO/INS odometry to estimate base station positions according to the model in Section V-A. Subsequently, UWB range residuals at each epoch are calculated based on estimated positions. The consistency of the current range with those from other epochs is then assessed by checking whether its residual is below a preset threshold, thereby enabling outlier detection and rejection.

The specific procedure of the RANSAC-based MODR method is shown in Fig. 3. First, relevant parameters are initialized, and a subset of N samples is randomly selected from the full set of UWB ranges D, where N is set to 70% of the total number of ranges in D. The base station position is then estimated using the ODO/INS relative poses following the method described in Section V-A. Next, theoretical ranges

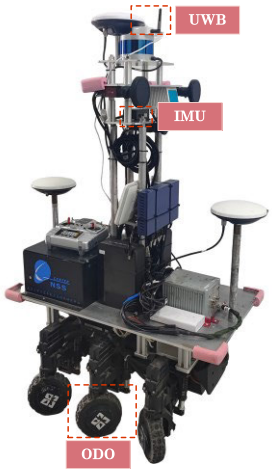

Fig. 4. Employed wheeled robot for real-world experiments.

(a) (b)

Fig. 5. Experimental environments and equipment. (a) Open LOS. (b) Complex indoor NLOS.

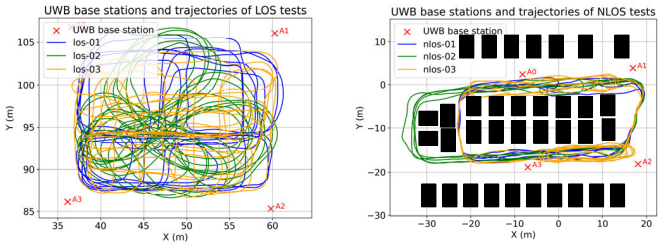

(a) (b)

Fig. 6. UWB base station distributions and test trajectories. Black rectangles represent vehicles and other obstacles. (a) Open LOS. (b) Complex indoor NLOS.

of all measurements except for the selected N samples are calculated based on the estimated position, and their residuals are then obtained. Measurements with residuals smaller than a preset threshold ϵ are classified as inliers, where the threshold ϵ is set to 0.05 m, enabling consistency checking of the UWB ranges. Then, the base station position is reestimated using both the new inliers and the original sampled inliers when their combined number exceeds M, where M is set to 85% of the total number of ranges in D. The sum of residual norms for these ranges is calculated based on the updated base station positions. This process is iterated multiple times. During each iteration, the base station position is updated, and the sum of residual norms is recalculated. Finally, the base station position estimation model with the minimum residual sum is chosen as the optimal model. The corresponding inlier set is regarded as the optimal UWB ranging dataset with outliers removed and is used for the state update.

VI. Experiments and Analysis

A. Experimental Setup

The employed wheeled robot for quantitative experiments is shown in Fig. 4. The used UWB module is the LD-150, which is based on the DW1000 chip and operates at a frequency of 5 Hz. The IMU is the ADIS16465 from ADI with a frequency of 200 Hz. The ODO velocity measurements are obtained from the wheel encoder of the robot chassis, which has a pulse per revolution of 800 and a frequency of 5 Hz. The ground-truth poses are obtained by matching the LiDAR data from the robot to a prebuilt point cloud map, with an accuracy of about 2 cm. The point cloud map is constructed via postprocessing using the commercial device RS100i-MT.

Two test environments are designed for comprehensive validation of the proposed method: an open LOS environment and a complex indoor NLOS environment. As shown in Fig. 5, the LOS environment is an open basketball court with minimal NLOS interference, which is used to evaluate the upper-bound positioning accuracy of our system. The complex indoor NLOS environment is in an underground garage with many obstacles. UWB ranges are severely affected by NLOS interference in this environment, resulting in numerous outliers. Thus, the NLOS environment is used to evaluate the robustness and accuracy of the proposed method under challenging conditions.

To eliminate the influence of base station distribution on positioning performance in both environments, the spatial distribution of base stations is kept consistent. Base stations are placed at the four corners of a 22 × 24 m rectangular area. The distances of A0–A1 and A2–A3 are about 24 m, while the distances of A0–A3 and A1–A2 are about 22 m. In each scenario, data from three test sequences were collected along different paths to reduce the impact of the path selection, and thus, the reliability of the results can be improved. The trajectories of each sequence and the base station distribution are shown in Fig. 6, where black rectangles represent vehicles and other obstacles. Among the NLOS sequences, the nlos-02 sequence experiences the strongest interference due to its proximity to a wall, which severely obstructs UWB signals and induces significant multipath effects. Fig. 7 presents two subplots analyzing the UWB measurements from the nlos-02 sequence. The top subplot displays the UWB range errors over time, while the bottom subplot shows the number of available UWB ranges at each epoch. For the error calculation, the ground-truth ranges were derived from ground-truth poses. Significant range errors and frequent measurement dropouts are observed due to NLOS interference.

The positioning accuracy is evaluated by comparing the estimated horizontal positioning results with the ground truth. The methods used for comparison are given as follows.

1) *MODR-UOINS:* The proposed tightly coupled UWB-ODO-INS with the proposed MODR method.
2) *OINS:* A subsystem of MODR-UOINS without using UWB for evaluating the positioning accuracy of the ODO/INS odometry; it does not use the MODR or

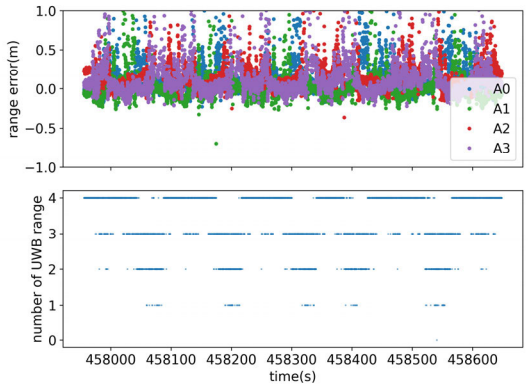

Fig. 7. UWB range errors and numbers on the nlos-02 sequence. The range number means the observed base station number in a UWB frame.

TABLE I
POSITIONING ERRORS IN THE OPEN LOS ENVIRONMENT

Error (m)	OINS		MODR-UINS		SODR-UOINS		ISM-UOINS		MODR-UOINS	
	RMSE	CEP95	RMSE	CEP95	RMSE	CEP95	RMSE	CEP95	RMSE	CEP95
los-01	0.694	1.445	**0.087**	0.148	0.088	0.150	0.091	0.156	0.088	**0.144**
los-02	1.500	3.097	**0.105**	**0.163**	0.114	0.185	0.110	0.173	0.106	0.166
los-03	1.448	2.624	0.112	0.182	0.110	0.186	0.106	0.174	**0.103**	**0.168**
RMS	1.269	2.488	0.102	0.165	0.105	0.174	0.103	0.168	**0.099**	**0.160**

The bold results demonstrate the best among these methods.

single-epoch outlier detection and rejection (SODR) methods, which are employed in this article only for UWB NLOS mitigation.

3) *MODR-UINS:* A variant of MODR-UOINS without ODO to evaluate the positioning accuracy of the tightly coupled UWB-INS.
4) *SODR-UOINS:* A variant of MODR-UOINS where the proposed MODR method is replaced by an SODR method, i.e., chi-square test.
5) *ISM-UOINS:* A variant of MODR-UOINS where the proposed MODR method is replaced by the innovation sequence monitoring (ISM) method [33].

B. Results and Discussion

1) Open LOS Environment: The positioning results are shown in Table I. The root mean square error (RMSE) and 95% circular error probable (CEP95) values for MODR-UOINS, MODR-UINS, ISM-UOINS, and SODR-UOINS are comparable, which is consistent with theoretical expectations. Under ideal LOS conditions, UWB provides high-accuracy absolute positioning and plays a dominant role in the positioning process. Therefore, fusing only UWB and IMU is sufficient to achieve high positioning accuracy. Due to the minimal NLOS interference in this open LOS environment, the role of outlier culling methods is significantly diminished. Consequently, the SODR, ISM, and MODR methods exhibit comparable performance. In contrast, OINS exhibits significantly larger errors, indicating that positioning based solely on ODO and IMU results in considerable drift accumulation. Thus, absolute positioning sensors such as UWB must be introduced to suppress the drift. Besides, the results demonstrate that MODR-UOINS achieves an upper-bound positioning accuracy of approximately 0.1 m. This value can serve as an important reference for evaluating the positioning performance of various methods in the complex indoor NLOS environment.

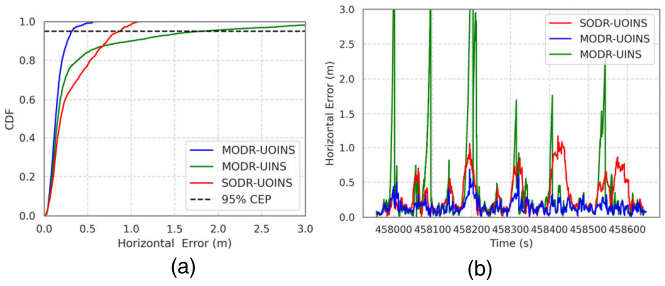

Fig. 8. Comparison of the positioning errors on the nlos-02 sequence. (a) CDFs of positioning error. (b) Positioning error.

TABLE II
POSITIONING ERRORS IN THE COMPLEX INDOOR NLOS ENVIRONMENT

Error (m)	MODR-UINS		SODR-UOINS		ISM-UOINS		MODR-UOINS (without OE)		MODR-UOINS	
	RMSE	CEP95	RMSE	CEP95	RMSE	CEP95	RMSE	CEP95	RMSE	CEP95
nlos-01	0.189	0.338	0.316	0.724	0.196	0.408	0.225	0.500	**0.141**	**0.254**
nlos-02	0.806	1.791	0.397	0.867	0.332	0.798	0.258	0.576	**0.166**	**0.317**
nlos-03	0.239	0.489	0.390	0.966	0.263	0.606	0.196	0.345	**0.153**	**0.261**
RMS	0.497	1.090	0.369	0.858	0.269	0.625	0.228	0.483	**0.154**	**0.279**

MODR-UOINS (without OE) refers to MODR-UOINS without online estimation of UWB ranging errors, as used in VI.C.3.

2) Complex Indoor NLOS Environment: Fig. 8 compares the positioning performance of various methods on the nlos-02 sequence using two subplots: Fig. 8(a) shows the cumulative distribution functions (CDFs) of the positioning errors, and Fig. 8(b) shows the corresponding time-series positioning error curves. As shown in Fig. 8(a), the cdf of positioning error for MODR-UOINS consistently lies entirely to the left of those for the other methods, indicating its higher positioning accuracy at any given probability level. The positioning error curves in Fig. 8(b) further corroborate this superiority. The error trajectory of MODR-UOINS not only remains lower than those of other methods for most of the duration but also exhibits significantly smaller fluctuations, indicating enhanced stability and robustness. In contrast, MODR-UINS exhibits the worst performance due to unsuppressed IMU drift, underscoring the inadequacy of relying solely on UWB and IMU in this complex NLOS environment. Therefore, incorporating ODO measurements is essential for suppressing IMU drift and thereby improving overall performance.

The positioning results are shown in Table II. The proposed MODR-UOINS achieves an overall RMSE of approximately 0.154 m, outperforming the other three methods. Notably, this performance is comparable to that obtained in the open

TABLE III
POSITIONING ERRORS UNDER THE DUAL BASE STATION CONDITION

Error (m)	MODR-UINS		SODR-UOINS		ISM-UOINS		MODR-UOINS	
	RMSE	CEP95	RMSE	CEP95	RMSE	CEP95	RMSE	CEP95
nlos-01	0.328	0.687	0.954	1.969	0.230	0.482	**0.166**	**0.330**
nlos-02	1.519	2.927	0.443	0.890	0.308	0.628	**0.184**	**0.344**
nlos-03	0.441	0.993	0.338	0.798	0.274	0.626	**0.161**	**0.282**
RMS	0.933	1.828	0.638	1.330	0.273	0.583	**0.171**	**0.320**

LOS environment, demonstrating that MODR-UOINS can effectively mitigate NLOS effects. Specifically, compared to SODR-UOINS, MODR-UOINS reduces RMSE and CEP95 by approximately 58.3% and 67.5%, respectively. This confirms the superiority of the proposed MODR method. In contrast, the performance of the SODR method degrades because it relies on an accurate absolute pose at the current time, which cannot be guaranteed in this NLOS environment. Compared to ISM-UOINS, MODR-UOINS reduces RMSE and CEP95 by approximately 42.8% and 55.4%, respectively. This is because single-frame outliers are not detected by ISM-UOINS when their innovations are too small to exceed the threshold during sliding-window averaging. Instead, MODR-UOINS detects outliers based on geometric consistency constraints, enabling more effective identification of these outliers. Furthermore, ISM-UOINS exhibits higher positioning accuracy than SODR-UOINS, indicating that persistent biases in UWB ranges can be effectively detected and rejected through multiepoch sequence innovation analysis. Compared with MODR-UINS, MODR-UOINS shows a reduction in RMSE and CEP95 of approximately 69.0% and 74.4%, respectively. This indicates that the ODO/INS odometry provides more accurate relative poses, thereby enhancing the effectiveness of the proposed MODR method.

C. Robustness Analysis

1) Impact of the Sparse Base Station Deployment: To evaluate the robustness of MODR-UOINS under sparse base station deployment, tests were conducted with only two base stations simultaneously visible. The positioning results of different methods in the complex indoor NLOS environment are shown in Table III. MODR-UOINS achieves an accuracy of 0.171 m using just two base stations, which is comparable to the 0.154 m obtained using four. This is because MODR-UOINS employs a tightly coupled strategy and applies the proposed MODR method to UWB ranges based on the sliding window strategy of MSCKF. Consequently, the method can effectively identify and reject outliers even under sparse base station deployment, thereby maintaining high positioning accuracy. These results also show that MODR-UOINS can reduce the deployment cost of base stations.

Besides, under dual base station conditions, MODR-UOINS achieves a more substantial improvement in positioning accuracy over SODR-UOINS, reducing RMSE and CEP95 by 73.2% and 75.9%, respectively. These reductions are greater than the 58.3% and 67.5% observed with four base stations. This indicates that the advantages of the proposed

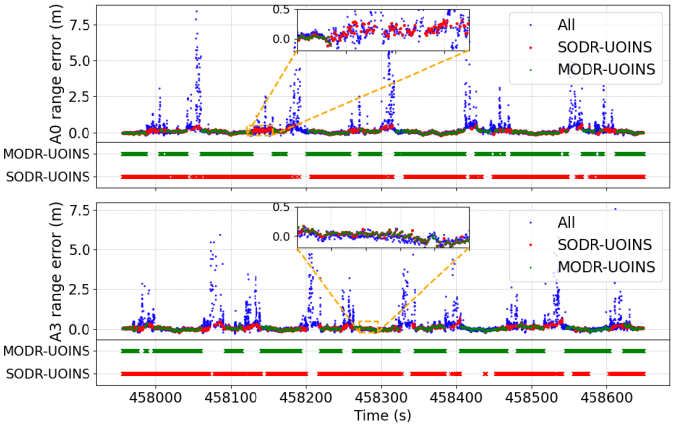

Fig. 9. Comparison of the outlier-culling performance on the nlos-02 sequence. Here, the "All" denotes the range errors between the raw ranges and the ground-truth ranges of UWB. The raw ranges are measured using the DS-TWR method, while the ground-truth ranges are derived from ground-truth poses. The A0 and A3 range errors refer to the range errors from UWB base stations 0 and 3, respectively. Since A0 and A3 are subject to stronger NLOS interference, only the range errors of these two base stations are presented.

MODR method become increasingly evident as the number of available UWB ranges decreases. This is mainly due to the different pose estimation strategies adopted by the two methods. MODR-UOINS relies on relative pose estimations from ODO/INS odometry and employs multiepoch outlier culling based on MSCKF, making it less sensitive to reductions in UWB base stations. In contrast, the SODR method depends on accurate absolute pose estimations, resulting in increased positioning errors when UWB ranges are limited.

2) Impact of the MODR Method: To provide an intuitive comparison of the two methods on the nlos-02 sequence, three types of range errors are plotted in the upper half of each subfigure, as shown in Fig. 9. These include: 1) errors between the raw UWB ranges and the ground-truth ranges; 2) errors between ranges retained after outlier culling by the SODR method and the ground-truth ranges; and 3) errors between ranges retained after outlier culling by the MODR method and the ground-truth ranges. The raw UWB ranges are measured using the DS-TWR method, while the ground-truth ranges are derived from ground-truth poses. In addition, green and red markers in the lower half of each subplot indicate whether the ranges at the corresponding time points are retained by MODR-UOINS and SODR-UOINS, respectively. A marker is plotted only if a range is retained, thereby illustrating which measurements are accepted by each method.

As shown in Fig. 9, SODR-UOINS retains some ranges with significantly large errors, resulting in more marker points and reflecting its failure to detect certain outliers. This limitation occurs because the SODR method relies solely on the current UWB ranges for outlier detection and rejection and requires accurate absolute poses. As a result, in complex NLOS environments where accurate absolute poses cannot be guaranteed, this method is prone to missing outliers, thereby limiting its positioning robustness and accuracy. In contrast, the proposed MODR method integrates historical range information and avoids reliance on absolute poses by utilizing

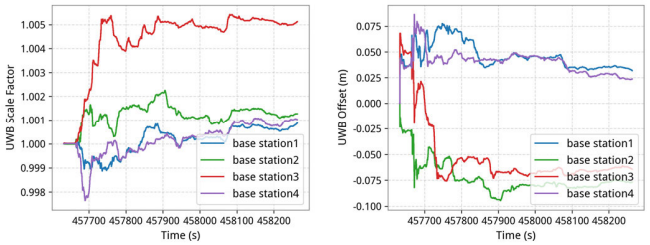

(a) (b)

Fig. 10. Estimated scale factors and offsets on the los-01 sequence. (a) Scale factors. (b) Offsets.

TABLE IV
EFFICIENCY AND POSITIONING RESULTS ON THE NLOS-02 SEQUENCE

Sliding window size	5	10	15	20	25
INS propagation time(ms)	1.48	2.04	2.83	3.87	5.17
UWB update time (ms)	0.10	0.15	0.31	0.54	0.89
MODR time (ms)	11.18	14.68	17.78	18.31	22.24
RMSE (m)	0.271	0.219	0.166	0.197	0.193

relative pose estimations from ODO/INS odometry. Thus, MODR-UOINS enables more effective detection and rejection of outliers, thereby significantly improving robustness in challenging indoor environments.

3) Impact of the Online UWB Ranging Error Estimation: The online estimation curves of the scale factors and offsets for each base station on the los-01 sequence are shown in Fig. 10, where significant fluctuations are observed at the initial stage. However, both parameters gradually converge over time, indicating that systematic UWB ranging errors are effectively compensated for during online estimation. To quantitatively evaluate the impact of online error estimation on positioning accuracy, the positioning accuracy of MODR-UOINS and MODR-UOINS (without OE) was compared. Here, MODR-UOINS (without OE) refers to MODR-UOINS without online estimation of UWB ranging errors. The test results are shown in Table II. Compared to MODR-UOINS (without OE), the RMSE and CEP95 of MODR-UOINS are reduced by approximately 32.5% and 42.2%, respectively. These results further confirm that online calibration of ranging errors can improve positioning accuracy.

4) Efficiency and Positioning Accuracy for Different Sliding Window Sizes: As shown in Table IV, the computational efficiency and positioning accuracy of MODR-UOINS were evaluated using different sliding window sizes on the nlos-02 sequence. As the window size increases, the INS propagation time, UWB update time, and MODR processing time increase accordingly. This indicates that larger windows require maintaining more historical states, which increases computational complexity. The RMSE initially decreases and then increases with window size, reaching a minimum at 15. A small window size provides insufficient historical information, leading to degraded positioning accuracy. Conversely, an excessively large window weakens state correlations and intensifies error accumulation, degrading positioning accuracy.

TABLE V
POSITIONING ERRORS UNDER DIFFERENT RANSAC THRESHOLDS

Error (m)	0.03		0.05		0.075		0.1		0.15	
	RMSE	CEP95	RMSE	CEP95	RMSE	CEP95	RMSE	CEP95	RMSE	CEP95
nlos-01	0.221	0.398	**0.141**	**0.254**	0.141	0.259	0.145	0.284	0.310	0.382
nlos-02	0.187	0.395	**0.166**	**0.317**	0.254	0.504	0.271	0.567	0.273	0.545
nlos-03	0.177	0.289	**0.153**	**0.261**	0.160	0.283	0.183	0.361	0.179	0.373
RMS	0.196	0.364	**0.154**	**0.279**	0.191	0.366	0.207	0.421	0.260	0.440

Therefore, a sliding window size of 15 is selected as it offers an optimal balance between computational efficiency and positioning accuracy. Besides, the average interval of the UWB frames is around 200 ms. The results in Table IV show that the average processing time of MODR-UOINS is significantly shorter than this interval, indicating excellent real-time capability. When the sliding window size is set to 15, MODR-UOINS can run at around nine times the real-time speed.

5) Impact of the RANSAC Threshold: The positioning results of MODR-UOINS under different RANSAC thresholds are shown in Table V. The results indicate that the positioning accuracy is sensitive to the RANSAC threshold. The optimal accuracy is achieved when the threshold is set to 0.05 m, which matches the standard deviation of the UWB ranging errors. This threshold setting enables effective outlier rejection while preserving sufficient valid measurements. A threshold that is too low leads to excessive rejection of UWB ranges, resulting in insufficient inliers and degraded accuracy. Conversely, an overly high threshold retains more outliers as inliers, thereby increasing measurement noise and degrading accuracy. Therefore, a RANSAC threshold of 0.05 m is selected for optimal positioning performance.

VII. CONCLUSION

This article proposes a robust tightly coupled UWB-ODO-inertial navigation method based on the MSCKF framework for complex indoor environments. The short-term high-accuracy relative poses from the ODO/INS odometry are fully used to verify the consistency of UWB ranges. Hence, the interference of the NLOS signal can be mitigated by the proposed RANSAC-based MODR method. Experiment results demonstrate that the proposed MODR-UOINS achieves an accuracy of about 0.15 m in the complex indoor NLOS environment, exhibiting superior robustness. Besides, MODR-UOINS maintains comparable performance when using only two base stations compared to the results using four base stations simultaneously. This work offers a reliable solution to meet the high-accuracy positioning needs of wheeled robots in complex indoor scenarios. In future research, we will explore how to mitigate NLOS by using the raw UWB observations, thereby further improving the positioning accuracy.

REFERENCES

[1] T. Fan, T. Zhang, H. Zhang, J. Mo, and X. Niu, "A double sideband combined tracking method for Galileo E5 AltBOC signals," *Satell. Navigat.*, vol. 4, no. 1, p. 27, Dec. 2023.

[2] I. Oppermann, M. Hämäläinen, and J. Iinatti, *UWB: Theory and Applications*. Hoboken, NJ, USA: Wiley, 2004.

[3] H. Tang, X. Niu, T. Zhang, Y. Li, and J. Liu, "OdoNet: Untethered speed aiding for vehicle navigation without hardware wheeled odometer," *IEEE Sensors J.*, vol. 22, no. 12, pp. 12197–12208, Jun. 2022, doi: 10.1109/JSEN.2022.3169549.

[4] J. Bi et al., "Precise step counting algorithm for pedestrians using ultra-low-cost foot-mounted accelerometer," *Eng. Appl. Artif. Intell.*, vol. 150, Jun. 2025, Art. no. 110619, doi: 10.1016/j.engappai.2025.110619.

[5] X. Liu, H. Huang, Y. Gu, J. Li, X. Zhang, and T. Liu, "Low-cost IMU-based system for automated Parkinson's subtype and stage classification to support precision rehabilitation," *IEEE Trans. Neural Syst. Rehabil. Eng.*, vol. 33, pp. 3421–3431, 2025, doi: 10.1109/TNSRE.2025.3603555.

[6] L. Pezenka and K. Wirth, "Reliability of a low-cost inertial measurement unit (IMU) to measure punch and kick velocity," *Sensors*, vol. 25, no. 2, p. 307, Jan. 2025, doi: 10.3390/s25020307.

[7] H. Tang, T. Zhang, X. Niu, J. Fan, and J. Liu, "Impact of the Earth rotation compensation on MEMS-IMU preintegration of factor graph optimization," *IEEE Sensors J.*, vol. 22, no. 17, pp. 17194–17204, Sep. 2022, doi: 10.1109/JSEN.2022.3192552.

[8] P. Yu, M. Liu, and Y. Chen, "Performance analysis of INS/ODO integrated navigation with different measurement models in GNSS denied environment," in *Proc. China Satell. Navigat. Conf. (CSNC)*. Singapore: Springer, 2022, pp. 341–354.

[9] L. Wang, X. Niu, T. Zhang, H. Tang, and Q. Chen, "Accuracy and robustness of ODO/NHC measurement models for wheeled robot positioning," *Measurement*, vol. 201, Sep. 2022, Art. no. 111720, doi: 10.1016/j.measurement.2022.111720.

[10] Z. Zhang, X. Niu, H. Tang, Q. Chen, and T. Zhang, "GNSS/INS/ODO/wheel angle integrated navigation algorithm for an all-wheel steering robot," *Meas. Sci. Technol.*, vol. 32, no. 11, Nov. 2021, Art. no. 115122, doi: 10.1088/1361-6501/ac17fb.

[11] M. A. Fischler and R. C. Bolles, "Random sample consensus: A paradigm for model fitting with applications to image analysis and automated cartography," *Commun. ACM*, vol. 24, no. 6, pp. 381–395, 1987.

[12] A. S. M. S. Sagar, T. Kim, S. Park, H. S. Lee, and H. S. Kim, "Relative-position estimation based on loosely coupled UWB-IMU fusion for wearable IoT devices," *Comput., Mater. Continua*, vol. 75, no. 1, pp. 1941–1961, 2023, doi: 10.32604/cmc.2023.035360.

[13] Y. Zhong, T. Liu, B. Li, L. Yang, and L. Lou, "Integration of UWB and IMU for precise and continuous indoor positioning," in *Proc. Ubiquitous Positioning, Indoor Navigat. Location-Based Services (UPINLBS)*, Mar. 2018, pp. 1–5, doi: 10.1109/UPINLBS.2018.8559718.

[14] K. Naheem and M. S. Kim, "A low-cost foot-placed UWB and IMU fusion-based indoor pedestrian tracking system for IoT applications," *Sensors*, vol. 22, no. 21, p. 8160, Oct. 2022, doi: 10.3390/s22218160.

[15] S. Zihajehzadeh, P. K. Yoon, and E. J. Park, "A magnetometer-free indoor human localization based on loosely coupled IMU/UWB fusion," in *Proc. 37th Annu. Int. Conf. IEEE Eng. Med. Biol. Soc. (EMBC)*, Aug. 2015, pp. 3141–3144, doi: 10.1109/EMBC.2015.7319058.

[16] B. V. Krishnaveni, K. S. Reddy, and P. R. Reddy, "Indoor positioning and tracking by coupling IMU and UWB with the extended Kalman filter," *IETE J. Res.*, vol. 69, no. 10, pp. 6757–6766, Oct. 2023.

[17] D. Feng, C. Wang, C. He, Y. Zhuang, and X.-G. Xia, "Kalman-filter-based integration of IMU and UWB for high-accuracy indoor positioning and navigation," *IEEE Internet Things J.*, vol. 7, no. 4, pp. 3133–3146, Apr. 2020, doi: 10.1109/JIOT.2020.2965115.

[18] K. Yang et al., "Research on UWB/IMU location fusion algorithm based on GA-BP neural network," in *Proc. 40th Chin. Control Conf. (CCC)*, Jul. 2021, pp. 8111–8116.

[19] H. Lv, X. Zheng, Y. Qi, and Y. Song, "UWB-IMU pose estimation for roadheader based on machine learning," in *Proc. 5th Int. Conf. Intell. Control, Meas. Signal Process. (ICMSP)*, May 2023, pp. 1153–1156.

[20] B. Chen and Q. Li, "Application of multi-sensor fusion in indoor 3D positioning of UAVs," *Sensor World*, vol. 28, no. 3, pp. 27–36, 2022.

[21] C. L. Xiao and Z. M. Zhang, "Indoor integrated positioning technology of UWB/INS based on improved cubature Kalman filter," *Appl. Sci. Technol.*, vol. 50, no. 6, pp. 69–75, Oct. 2023, doi: 10.11991/yykj.202212018.

[22] Q. Zheng et al., "Channel non-line-of-sight identification based on convolutional neural networks," *IEEE Wireless Commun. Lett.*, vol. 9, no. 9, pp. 1500–1504, Sep. 2020.

[23] J. Fontaine, M. Ridolfi, B. Van Herbruggen, A. Shahid, and E. De Poorter, "Edge inference for UWB ranging error correction using autoencoders," *IEEE Access*, vol. 8, pp. 139143–139155, 2020.

[24] W. Zhu et al., "Improved indoor positioning model based on UWB/IMU tight combination with double-loop cumulative error estimation," *Appl. Sci.*, vol. 13, no. 18, p. 10046, Sep. 2023, doi: 10.3390/app131810046.

[25] J. Ding et al., "Combined UWB and IMU based mobile platform localization method for protected horticulture," *Trans. Chin. Soc. Agric. Eng.*, vol. 41, no. 1, pp. 1–11, 2025, doi: 10.11975/j.issn.1002-6819.202409099.

[26] T. Zhang, M. Yuan, L. Wei, Y. Wang, H. Tang, and X. Niu, "MR-ULINS: A tightly-coupled UWB-LiDAR-inertial estimator with multi-epoch outlier rejection," *IEEE Robot. Autom. Lett.*, vol. 9, no. 12, pp. 11786–11793, Dec. 2024, doi: 10.1109/LRA.2024.3498780.

[27] Z. Chen, A. Xu, X. Sui, Y. Hao, C. Zhang, and Z. Shi, "NLOS Identification- and correction-focused fusion of UWB and LiDAR-SLAM based on factor graph optimization for high-precision positioning with reduced drift," *Remote Sens.*, vol. 14, no. 17, p. 4258, Aug. 2022, doi: 10.3390/rs14174258.

[28] H. P. Yuan, X. R. Wang, and Q. Y. Li, "Full-rank decomposition and generalized inverse of row (column) skew-symmetric matrices," *J. Math.*, vol. 29, no. 4, pp. 513–518, 2009.

[29] T. D. Barfoot, *State Estimation for Robotics*. Cambridge, U.K.: Cambridge Univ. Press, 2024.

[30] D. Neirynck, E. Luk, and M. McLaughlin, "An alternative double-sided two-way ranging method," in *Proc. 13th Workshop Positioning, Navigat. Commun. (WPNC)*, Oct. 2016, pp. 1–4.

[31] A. Alarifi et al., "Ultra wideband indoor positioning technologies: Analysis and recent advances," *Sensors*, vol. 16, no. 5, p. 707, May 2016, doi: 10.3390/s16050707.

[32] A. Fischer, A. F. Izmailov, and M. V. Solodov, "The Levenberg–Marquardt method: An overview of modern convergence theories and more," *Comput. Optim. Appl.*, vol. 89, no. 1, pp. 33–67, Sep. 2024.

[33] P. D. Groves, *Principles of GNSS, Inertial, and Multi-Sensor Integrated Navigation Systems*, 2nd ed., Norwood, MA, USA: Artech House, 2015.